Supplemental Document

Optics EXPRESS

Standalone, CMOS-based Faraday rotation in a silicon photonic waveguide: supplement

YANNICK D'MELLO,[1,*] SANTIAGO BERNAL,[1] ADAM HELMY,[1] ESSAM BERIKAA,[1] OLIVIER CARPENTIER,[1] IMTIAZ ALAMGIR,[1] MD SAMIUL ALAM,[1] ESLAM EL-FIKY,[1,2] AND DAVID V. PLANT[1]

[1]*Department of Electrical and Computer Engineering, McGill University, Montreal, Quebec, Canada*
[2]*Electrical Engineering Department, Alexandria University, Alexandria, 21544, Egypt*
[*]*Yannick.DMello@mail.McGill.ca*

Supplement DOI: https://doi.org/10.6084/m9.figshare.19920206

Parent Article DOI: https://doi.org/10.1364/OE.453840

Standalone, CMOS-based Faraday rotation in a silicon photonic waveguide: supplemental document

Yannick D'Mello[1,*], Santiago Bernal[1], Adam Helmy[1], Essam Berikaa[1], Olivier Carpentier[1], Imtiaz Alamgir[1], Md Samiul Alam[1], Eslam El-Fiky[1,2], and David V. Plant[1]

[1]*Department of Electrical and Computer Engineering, McGill University, Montreal, Quebec, Canada.*
[2]*Electrical Engineering Department, Alexandria University, Alexandria, 21544, Egypt*
**Yannick.DMello@mail.McGill.ca*

1. Polarization Mode Conversion in the Waveguide

A particle of charge q traveling through an electromagnetic field at a velocity $\vec{v}$ experiences a Lorentz force $\vec{F}$ as it interacts with electric and magnetic fields, $\vec{E}$ and $\vec{B}$, respectively, such that,

$$\vec{F} = q(\vec{E} + \vec{v} \times \vec{B}) \qquad \text{(S1)}$$

The force exerted by the magnetic field depends on the direction of propagation of the particle relative to the field lines. In a material, electrons are loosely bound to the nuclei of atoms. Their response to applied forces determines the bulk response of the material. For example, electron oscillations can be induced by an electromagnetic wave propagating through the material. The nature of the oscillations depends on the response of the electrons to the physical properties of the wave. Additionally, if a magnetic field is applied to the material, the electrons would be subjected to the forces in equation (S1), which would change their response to the electromagnetic wave. In this manner, the optical properties of a material can be modified by the application of a magnetic field.

In the case of linearly polarized light, the Lorentz force manifests as a rotation of its plane of polarization inside a material. Note that linearly polarized light is a superposition of left and right circularly polarized components which add along the plane of polarization and cancel along the transverse plane. Under an applied magnetic field, the difference in velocities between these components rotates the plane of polarization and is known as Faraday rotation. Since the angle of rotation, θ, depends on the direction of the B field lines relative to the propagation direction, the effect is nonreciprocal. It is determined by the direction of propagation of light with respect to the applied B field along an interaction length, l, such that,

$$\theta = VBl \qquad \text{(S2)}$$

The Verdet constant, V, is the magneto-optic property of the material that determines the interaction strength. Since the rotation θ is the primary figure of merit for the performance of a Faraday rotator, methods to maximize each of its three parameters were investigated in this work. Figure S1 illustrates this concept.

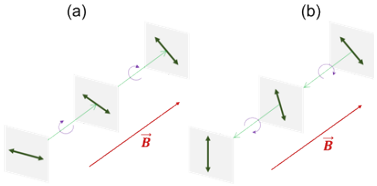

Fig. S1. Schematic of Faraday rotation illustrating non-reciprocal polarization rotation (violet). (a) clockwise rotation of the plane of polarization of light when propagating (green) in the direction of the magnetic field (red) and (b) counter-clockwise rotation when propagating in the opposite direction.

The Verdet constant of a material is determined by its dispersion and scaled by the charge-to-mass ratio of the electrons. It is described by the Becquerel equation [1],

$$V = \frac{q_\mathrm{e}}{m_\mathrm{e} c_0^2} \cdot \frac{\lambda_0}{2} \cdot \left(\frac{dn_\mathrm{eff}}{d\lambda}\right) \tag{S3}$$

Where q_e and m_e are the charge and mass of an electron (q_e is a negative quantity), c_0 is the speed of light, λ_0 is its vacuum wavelength, and n_eff is the effective index of the optical mode. The dispersion $\mathrm{d}n_\mathrm{eff}/\mathrm{d}\lambda$ induced by the material could be modified by its geometry. This parameter was investigated by fabricating different waveguide cross-sections. In a single-mode waveguide, Faraday rotation causes NR PMC [2] between the TE_0 and TM_0 modes. However, the asymmetric cross-section of SiP waveguides results in two different n_eff for the two modes, and as such, two different propagation constants, β_TE0 and β_TM0. This causes a π phase mismatch at every half-beat length [3],

$$l_\mathrm{HB} = \frac{\pi}{|\beta_{TE0} - \beta_{TM0}|} = \frac{\lambda}{2|n_\mathrm{eff,TE0} - n_\mathrm{eff,TM0}|} \tag{S4}$$

The phase mismatch reduces the efficiency of PMC by limiting energy transfer between the modes. Essentially, mode beating causes a polarization state evolution which can be tracked using an averaged Stokes vector on the Poincaré sphere [4]. It can be mitigated by periodically reversing the magnetic field to allow quasi-phase matching (QPM) between the modes [5, 6]. The electromagnetic coil in this investigation was designed to produce such a B-field reversal.

2. Generation of an Electro-Magnetic Field

The magnetic flux, Φ_B, interacting with the mode is determined by the flux density, B, overlapping with the cross-sectional area, A_mode, of the optical mode,

$$\Phi_\mathrm{B} = BA_\mathrm{mode} \tag{S5}$$

The rotation of the mode could be determined by the magnetic flux density that overlaps with the Poynting vector at each point in the mode field distribution. In this design, the magnetic field was generated by an electric current, I, in a coil of n windings or turns. The magnetic flux density produced by the coil was,

$$B = \mu_0 \mu_r \frac{nI}{l_{coil}} \tag{S6}$$

Where μ_r is the relative magnetic permeability of the materials through which the flux is being evaluated and μ_0 is the permeability of free space. Since the length of the coil, l_{coil}, determined the strength of the magnetic field, different coil lengths were designed. The magnetic field in the waveguide was also directly proportional to the current through the coil.

Out of the materials available on-chip, Al and TiN are paramagnetic with susceptibilities of 1.7×10^{-5} cm^3/mol and 38×10^{-6} cm^3/mol, respectively. On the other hand, Si and SiO_2 are diamagnetic with susceptibilities of -3.9×10^{-6} cm^3/mol and -29.6×10^{-6} cm^3/mol, respectively. To compensate for the expulsion of the magnetic field by Si and SiO_2, two Al and two TiN layers were deposited co-axially inside the coil to emulate a solenoid core.

3. Resistive Heating in the Coil

The resistance of each winding of the coil was a summation of resistances in series formed by the resistance of each layer and the ohmic contacts between them. A larger current would produce a larger current density, J, which generated resistive or Joule heat, Q, from the components of the coil,

$$Q = \rho(T)|J|^2 \tag{S7}$$

Since the same coil design was used for every device, the evolution of cross-sectional area along the path of electrical current was consistent for a coil length l with an integer number of

turns n. Its average resistivity was therefore equivalent to its resistance, R, per unit length of wiring as $R/L = \rho/A$. The electrical resistivity $\rho(T)$ increases with temperature,

$$\rho(T) = \rho_0(1 + \alpha(T - T_0)) \quad \text{(S8)}$$

Where α is the temperature coefficient of resistivity and T_0 is the room temperature at 293.15 K. Resistive heating in the coil was therefore be measured by the relationship between its resistance per unit length and the input current.

4. Inductance of the Coil

The maximum operating frequency of the coil was determined by its inductive reactance or impedance,

$$Z_L = r + 2\pi fL \quad \text{(S9)}$$

Where L is its inductance. In this design, R was assumed to be the DC circuit load in a standard RL series circuit. The inductance, L, of the coil was,

$$L = \frac{n\Phi_{\mathrm{B,coil}}}{I} = \mu_0\mu_r\frac{n^2A_{\mathrm{coil}}}{l} \quad \text{(S10)}$$

The inner width of the coils was 13.7 μm or 14.7 μm, resulting in an A_{coil} of 34.66 μm^2 or 37.19 μm^2, respectively. Using equation (S10), these dimensions resulted in the inductances shown in Table S1.

Table S1. Inductance of the six fabricated SiP coils as per design variations.

Gap \ Length	**l = 492.9 μm** **n = 53**	**l = 744 μm** **n = 80**	**l = 1097.4 μm** **n = 118**
g = 0.5 μm	248.2 μH	374.7 μH	552.6 μH
g = 1 μm	266.3 μH	402 μH	593 μH

The response time of the circuit to a change in current could be determined from its time constant [7],

$$\tau = L/R \quad \text{(S11)}$$

Here, R was obtained from the measured resistance per unit length. This resulted in transient times of 196.3 fs and 210.6 fs for coils with a w_{gap} of 0.5 μm and 1 μm, respectively. The response would reach steady state at approximately 5τ, which represented the transient time and indicated its behaviour as a low pass filter. It corresponds to operating frequencies of 2.547 THz and 2.374 THz.

5. Characterization of Design Variations

This device design investigated the feasibility of inducing NR PMC via Faraday rotation in the SiP platform. It was based on the operating principle of conventional bulk isolators, in which optical nonreciprocity was induced by rotating the plane of polarized light under an applied magnetic field. As per equation (S2), the angle of rotation θ was dependent on the magnetic flux density in the direction of propagation B_Y, the Verdet constant of the mode V, and the MO interaction length l_{MO}.

Four variations of waveguides were designed for characterization purposes. The baseline was a Si strip waveguide with a width of 500 nm and height of 220 nm. This base design was modified to produce 15 device variations including a reduced gap of 500 nm between the Si layers, 3 coil lengths (492.9 μm, 744 μm, and 1097.4 μm, which accommodated 53, 80, and 118 windings, respectively), and 4 waveguide types (strip, slot, doped with Boron, or doped with Phosphorus). The slot waveguide consisted of 180 nm wide sidewalls on either side of a 180 nm

wide slot. To vary the refractive index, the Si waveguide was also doped with Phosphorus (n-Si) and Boron (p-Si). Overall, fifteen variations were fabricated including four types of waveguides surrounded by two different coil widths spanning three coil lengths of 493 µm, 744 µm, and 1097 µm. The parameter values are listed in Table S2 for each device.

Table S2. Parameters of the design variations that were fabricated on-chip.

#	Length (µm)	Separation (µm)	Doping	Slots
1	492.9	1	-	0
2	492.9	0.5	n	0
3	492.9	0.5	p	0
4	492.9	0.5	-	1
5	492.9	0.5	-	0
6	744	1	-	0
7	744	0.5	n	0
8	744	0.5	p	0
9	744	0.5	-	1
10	744	0.5	-	0
11	1097.4	1	-	0
12	1097.4	0.5	n	0
13	1097.4	0.5	p	0
14	1097.4	0.5	-	1
15	1097.4	0.5	-	0

The design layout is shown in Figure S2 in the form of photographs of the on-chip devices.

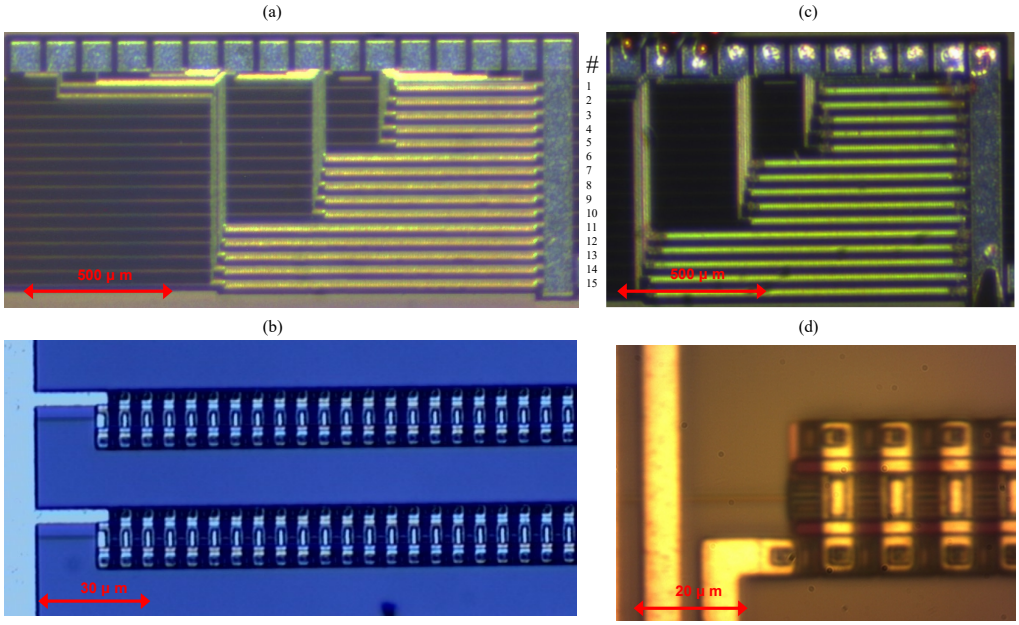

Fig. S2. Top-down photographs of (a) the fabricated SiP chip with 15 variations of the device design as described in Table S2, (b, d) zoom-in of the devices, (c) the coils after breakdown. The different colours are due to the combination of microscope and illumination which was optimized for each image.

The waveguides were extended to the ends of the chip and connected to input/output edge couplers. The edge couplers were 60 µm long and linearly tapered from a width of 500 nm to 180 nm at the edge of the chip. Edge couplers offer a lower polarization sensitivity than vertical couplers, which would allow both TE and TM polarizations to be coupled to the device.

Coils with a 1 µm gap did not have a measurably higher resistance than those with a 0.5 µm gap. This is because the extra width was achieved by elongating the Al strips above the waveguide and their conductivity was higher than the other materials of the coil by orders of magnitude. Note that although the cross-sectional area could be increased without incurring a significantly higher resistance, the inductance (and therefore response time) would be proportionally increased.

A low dopant concentration was chosen to minimize absorption loss. However, such light doping induced only a negligible difference in effective index i.e., $\Delta n_{\mathrm{eff}}/n_{\mathrm{eff}} \rightarrow 0$. As a result, the mode profiles of the p-Si and n-Si waveguides were almost the same as the undoped Si waveguide. Consequently, their Verdet constant was equivalent to the undoped waveguides. Therefore, these two waveguide types were excluded from the remaining analysis. Fundamental TE and TM mode profiles for the strip and slot waveguides are shown in Figure S3 at a wavelength of 1550 nm. At a wavelength of 1310 nm, mode field distributions were more confined but retained their profile. Doping the waveguides with either P or B did not significantly alter the refractive index of the Si waveguide and consequently the Verdet constant. As a result, they did not offer a significant performance variation from the base design and were not evaluated further.

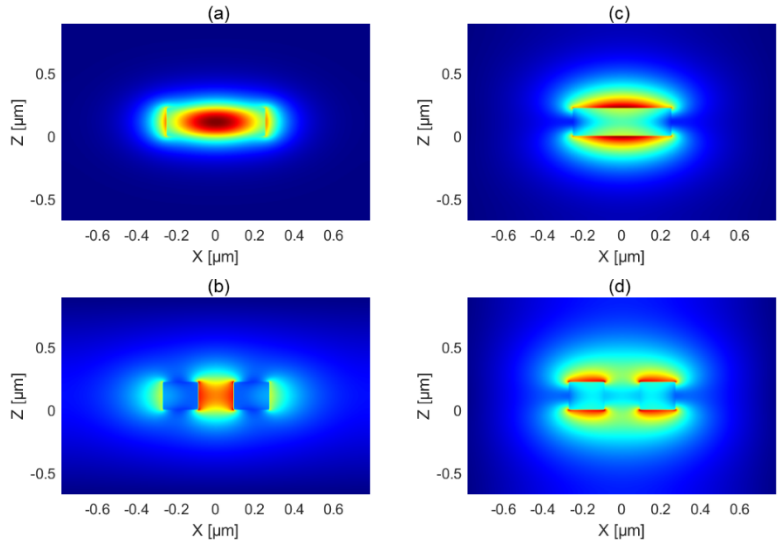

Fig. S3. Distribution of the electric field magnitudes at a wavelength of 1550 nm. TE_0 mode in the (a) strip and (b) slot waveguide, and TM_0 modes in the (c) strip and (d) slot waveguide.

The effective index for each mode across the 1260-1600 nm wavelength range is shown in Figure S4(a). The right axis shows the corresponding half-beat length between both orthogonal modes for each waveguide type. Chromatic dispersion at a given wavelength was calculated as the slope of the modal effective index. Using this, the Verdet constant of each mode was calculated as shown in Figure S4(b). The effect of overlap between the evanescent field of the waveguide modes and the lower Al strip was neglected.

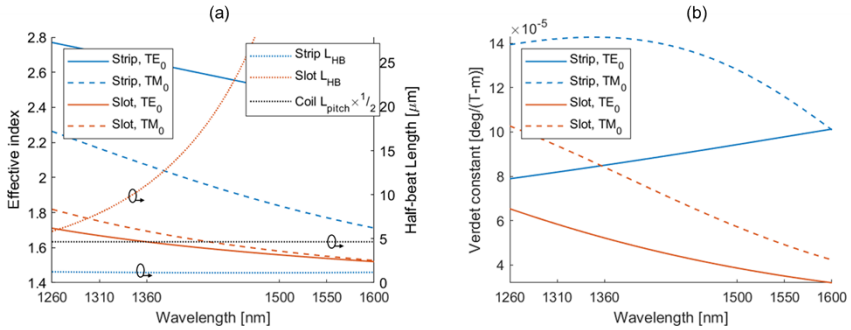

Fig. S4. Characterisation of different modes under study at different wavelengths. (a) Effective index of the TE_0 and TM_0 modes in strip and slot waveguides (solid and dashed lines, left axis) and the half-beat length between the fundamental modes of the slot and strip waveguides (dotted lines, right axis). The half-pitch length of the coil is also shown for reference. (b) Verdet constant for the same two fundamental modes of each waveguide type.

For a strip waveguide, the n_{eff} for the TE_0 mode was higher than that of the TM_0 mode, which corresponded to its larger width in comparison to its height. For a slot waveguide, however, the effective index of the TM_0 mode was higher than TE_0. This Δn decreased to almost zero at 1600 nm, which produced an asymptotic increase in the corresponding half-beat length, L_{HB}, thereby precluding the need for QPM. At shorter wavelengths, the L_{HB} was almost equal to the pitch of the coil, which would maximize QPM. The effective index difference between the orthogonal waveguide modes resulted a wide range of half-beat lengths. A mismatch between the half-beat length and the coil pitch would reduce PMC efficiency [4]. Perfect phase

matching was exhibited for longer wavelengths in the slot waveguide, which indicated the possibility of not requiring mode beating. However, the PMC efficiency might still be reduced by the mismatched coil pitch. In future iterations of the waveguide design, the half-beat length between modes could be matched with the pitch of the coil to ensure QPM for a suitably dispersion engineered [8] waveguide mode.

Although the intensity of the TE mode is indeed stronger inside the Si core layer than the TM mode, note that Faraday rotation did not depend on the intensity of light. Additionally, as per equation (S3), the interaction depended on the dispersion of the mode (via the Verdet constant) rather than the effective index itself. Although the interaction also depended on the magnetic permeability of the materials, the magnetic permeability of Si and SiO_2 were similar enough that they did not affect the rotation of the TE mode (which was more concentrated in the Si core layer) more than the TM mode. So, the extent of Faraday rotation of the mode depended on its Verdet constant more than its field distribution in the core. Since the Verdet constant of the TE mode was lower than the TM mode, its corresponding Faraday rotation effect was weaker as seen in Table S3.

Table S3. Rotation of the polarization state for the evaluated devices. The first column indicates the device number (#) corresponding to Table S2, which also implies the type of waveguide used. Values are shaded from white to green to reflect the smallest to largest angles of rotation.

Device #	**Rotation (pico-degrees)**			
$\lambda \rightarrow$	*1310 nm*		*1550 nm*	
Mode $\rightarrow$	TE_0	TM_0	TE_0	TM_0
1	12.15	21.07	14.48	17.33
4	8.66	13.91	5.2	7.29
5	12.14	21.05	14.47	17.31
6	18.4	31.91	21.94	26.25
9	13.12	21.06	7.87	11.04
10	18.39	31.89	21.92	26.22
11	27.2	47.18	32.43	38.8
14	19.39	31.14	11.64	16.32
15	27.18	47.13	32.4	38.76

The lowest rotation of 5.2×10^{-12} ° was obtained for the TE_0 mode of the slot waveguide at 1550 nm. The interaction was evaluated using the magnetic field strength along the centerline of the waveguide. Accuracy could be improved by integrating the magnetic field at each point in its overlap with the mode field distribution and over all three axes separately.

6. Vertical Axis Coils

To reduce the number of layers per winding, vertical-axis coils were also fabricated and tested. These coils employed multiple windings in a single layered spiral before connecting to the next metallization layer, which was also a spiral. The large area and negligible length of these coils resulted in such a high inductance that the response time was on the order of seconds. Since they could only be operated in steady state, they were deemed infeasible for commercial use.

7. Additional Methods

7.1 Layout Design for Device Fabrication

The chip layout was developed in Mentor Graphics Pyxis and verified in KLayout. The vertical windings of the coil were constructed from a stack of horizontal material layers that were

available through the standard chip fabrication process offered by the IME foundry (now AMF). Design parameters were constrained by the fabrication process. The material layers consisted of Si for the waveguides, doped n-Si for electrical wiring in the Si layer, two Al metallization layers for the electrical wiring and solenoid core, TaN for vias between the Si and Al layers, and TiN for an additional solenoid core.

7.2 Electrical Measurements of the Coils

All 15 coils were connected to a common ground which was accessed by a single bond pad. This required only one of the electrical probes to be moved to test a new device. For the measurement, each device was probed across its dedicated DC bond pad and the common ground. An ammeter was connected in series with the probing setup to measure the input current through the device. A power supply and oscilloscope were connected across the setup and ammeter. A voltage difference of up to 145 V was applied across this series connection and measured by the oscilloscope. For each device, the applied voltage was increased in steps of 1 V up to 40 V and beyond 120 V. In the range of 40-120 V, the resistance was more insensitive, which justified a larger step size of 5-10 V. The input voltage was increased until breakdown occurred, which was identified by a spark in the chip and an open circuit with negligible input current as shown in Figure S2(c).

7.3 Simulations

The mode field distributions for each waveguide were simulated in Lumerical Mode. Wavelength-dependent refractive indices were used for the Si core and SiO_2 cladding as obtained from the material database [9]. These points were fitted with a multi-coefficient model using the values ranging from 1200 nm to 1800 nm and a fit tolerance of 0.01.

Resistive heating was simulated using the ‘Electromagnetic Heating’ Multiphysics module in COMSOL Multiphysics, which combined the ‘Electric Currents’ and ‘Heat Transfer in Solids’ modules. The device layout was imported using the ‘ECAD Import’ module and each layer was projected to 3D by specifying its elevation, thickness, and material properties. Two cylindrical Al rods were added to the end terminals of the coil to connect it to the outer surface of the simulation region and send a current through the device.

This electromagnetic coil was simulated using the ‘Magnetic and Electric Fields’ module in COMSOL Multiphysics. All domains associated with the coil were added to the ‘Ampere’s Law and Current Conservation’ node to electrically connect them. The waveguide, cladding, and all four paramagnetic cores were added to the Ampere’s Law node to evaluate the magnetic field through these domains. The input current was swept over a range of 2-14 mA, which generated a magnetic field based on the magnetic permeability, electric permittivity, and conductivity of each material. Due to the low magnetic susceptibilities of Si and SiO_2, the magnetic field distribution was almost continuous across the mode profile within the region in and around the waveguide. Hence, the magnetic flux density in the waveguide was evaluated along a straight line through the center of the waveguide rather than at every point in the cross-section.

The magneto-optic interaction between the electrically generated magnetic field and confined optical modes was calculated in MATLAB. The angle of rotation was determined from equation (S2) using calculations of V and B_Y in the Supplementary Information. To determine the extent of Faraday rotation induced in the design, polarization rotation was simulated for a propagation length of 51.5 μm to minimize computation time. These results were then extrapolated to the fabricated device lengths.

References

1. R. Serber, "The Theory of the Faraday Effect in Molecules," Physical Review **41**, 489-506 (1932).
2. S. Wang, J. D. Crow, and M. Shah, "Thin-Film Optical-Waveguide Mode Converters Using Gyrotropic and Anisotropic Substrates," Applied Physics Letters **19**, 187-189 (1971).
3. S. Wang, M. Shah, and J. D. Crow, "Studies of the Use of Gyrotropic and Anisotropic Materials for Mode Conversion in Thin-Film Optical-Waveguide Applications," Journal of Applied Physics **43**, 1861-1875 (1972).

4. D. C. Hutchings and B. M. Holmes, "A Waveguide Polarization Toolset Design Based on Mode Beating," IEEE Photonics Journal **3**, 450-461 (2011).
5. D. C. Hutchings, B. M. Holmes, C. Zhang, P. Dulal, A. D. Block, S. Sung, N. C. A. Seaton, and B. J. H. Stadler, "Quasi-Phase-Matched Faraday Rotation in Semiconductor Waveguides With a Magnetooptic Cladding for Monolithically Integrated Optical Isolators," IEEE Photonics Journal **5**, 6602512-6602512 (2013).
6. D. C. Hutchings, "Prospects for the implementation of magneto-optic elements in optoelectronic integrated circuits: a personal perspective," Journal of Physics D: Applied Physics **36**, 2222-2229 (2003).
7. E. Tutorials, "Inductor - LR circuits", retrieved 13 July 2020, https://www.electronics-tutorials.ws/inductor/lr-circuits.html.
8. Y. D'Mello, O. Reshef, S. Bernal, E. El-fiky, Y. Wang, M. Jacques, and D. V. Plant, "Integration of Sub-wavelength, Periodic Structures in Silicon-on-Insulator Photonic Device Design," in *IET Optoelectronics,* (Institution of Engineering and Technology, 2020), pp. 125-135.
9. E. D. Palik, *Handbook of optical constants of solids* (Academic press, 1998), Vol. 3.